Cohort-based multiscale analysis of hemodynamic-driven growth and remodeling of the embryonic pharyngeal arch arteries

Stephanie E. Lindsey[1,*], Jonathan T. Butcher[1,‡,§] and Irene E. Vignon-Clementel[2,3,‡,§]

ABSTRACT

Growth and remodeling of the primitive pharyngeal arch artery (PAA) network into the extracardiac great vessels is poorly understood but a major source of clinically serious malformations. Undisrupted blood flow is required for normal PAA development, yet specific relationships between hemodynamics and remodeling remain largely unknown. Meeting this challenge is hindered by the common reductionist analysis of morphology to single idealized models, where in fact structural morphology varies substantially. Quantitative technical tools that allow tracking of morphological and hemodynamic changes in a population-based setting are essential to advancing our understanding of morphogenesis. Here, we have developed a methodological pipeline from high-resolution nano-computed tomography imaging and live-imaging flow measurements to multiscale pulsatile computational models. We combine experimental-based computational models of multiple PAAs to quantify hemodynamic forces in the rapidly morphing Hamburger Hamilton (HH) stage HH18, HH24 and HH26 embryos. We identify local morphological variation along the PAAs and their association with specific hemodynamic changes. Population-level mechano-morphogenic variability analysis is a powerful strategy for identifying stage-specific regions of well and poorly tolerated morphological and/or hemodynamic variation that may protect or initiate cardiovascular malformations.

KEY WORDS: Aortic arches, Chick embryo, Computational modeling, Heart development, Hemodynamics, Mechanical forces

INTRODUCTION

Congenital heart defects (CHDs) constitute the most severe form of a birth defect, accounting for 24% of deaths from developmental abnormalities (Mozaffarian et al., 2016). Abnormal pharyngeal arch artery (PAA) morphogenesis is associated with over 50% of clinically presented congenital heart defects (Go et al., 2013). Hemodynamics and proper flow patterns during cardiac development have been acknowledged as major drivers of vascular growth and remodeling (Lin and Taber, 1995; Jaffee, 1965; Taber and Eggers, 1996). Blood flow and its associated forces determine the mechanical environment of a subject, which in turn has implications at the cellular and molecular level. Wall shear stress (WSS) is sensed by endothelial cells and has been shown to regulate vascular remodeling (Brownlee and Langille, 1991; Kamiya and Togawa, 1980; Langille and Donnell, 1986), though exact thresholds for such changes are likely regional and stage specific. Pressure has been shown to modulate vessel shape and stretch (Banerjee et al., 2015; Taber, 1995; Li et al., 2004). Both mechanical and epigenetic perturbations in flow have been implicated in various congenital heart defects (Hu et al., 2009; Sedmera et al., 1999; Yashiro et al., 2007), including aberrant development of the great vessels (Abu-issa et al., 2002; Hogers et al., 1997, 1999; Rychter, 1962; Wendling et al., 2000). Yet despite all these associative relationships, the numeric relationship between mechanical forces and abnormal morphology, particularly at embryonic stages, has remained elusive. The difficulty of this quantification can be attributed to a lack of cohort-based analysis in numerical studies designed to quantify in vivo findings in which ranges for norms are reported. In order to render early CHD risk assessment and intervention possible, there is a need to establish cohort-based variations in flow and morphology. Only after the establishment of such a range will we as a field be able to assess its connection to malformation risk.

To date, quantitative studies of PAA development rather than qualitative surveys of PAA morphology are few (Hu et al., 2009; Kowalski et al., 2014; Leatherbury et al., 1990a,b; Lindsey et al., 2015; Wang et al., 2009). Leatherbury et al. (1990a,b) assessed PAA function through microcinephotography images and pressure and diameter measurements at the level of the ventricle and dorsal aorta (DoA), coupled with qualitative observations of the arches themselves. Hu et al. (2009) reported HH24 pulsatile Doppler flow measurements for PAA III and IV pairs, but were unable to measure the PAA VI pair owing to its position in the pharyngeal mesenchyme. No other published reports of experimentally measured PAA individual arch artery velocities exist. Similarly, in vivo pressure measurements have been limited to the DoA (Yoshigi et al., 2000; Zahka et al., 1989). Computational examinations of the arch arteries (Kowalski et al., 2012, 2013; Lindsey et al., 2015; Wang et al., 2009) have quantified blood flow and spatial variations in WSS across the entire PAA system but have not reported pressure maps. Based on idealized composite models, those studies elucidated the global role of flow and WSS in embryonic heart development but not local subject-specific hemodynamics that could reveal potential zones of high or low variability. The PAA network with its three lateral arch pairs serves as a highly informative model for quantitative variability studies, both locally, via segment by segment quantification across arches, and globally, via comparisons between embryos.

Before formation of the pulmonary artery and aortic arch, blood exits the heart through six bilaterally paired pharyngeal arch arteries. Growth and remodeling of these vessels consist of a complex sequence of events that involves the emergence, disappearance, elongation, rotation and twisting of the arch pairs, as they remodel into their mature adult forms. In the chick embryo, the process of

[1]Nancy E. and Peter C. Meinig School of Biomedical Engineering, Ithaca, NY 14850, USA. [2]INRIA Centre de recherche de Paris, Paris 75012, France. [3]Laboratoire Jacques Louis Lions, Sorbonne Universités UPMC, Paris 75005, France.
*Present address: PhyMedExp, Université de Montpellier, INSERM, CNRS - 371 avenue du Doyen Gaston Giraud, 34295 Montpellier, France.
‡These authors contributed equally to this work

§Authors for correspondence (irene.vignon-clementel@inria.fr; jtb47@cornell.edu)

J.T.B., 0000-0002-1894-4419; I.E.V.-C., 0000-0001-9754-4386

growth to maturation of the arch pairs largely occurs over the course of 7 days. The mature pulmonary artery and aortic arch are present by HH36 (day 10). Throughout maturation of the arch arteries, three of the six arch pairs persist: PAA III, PAA IV and PAA VI. These final arch pairs are present by HH24 (day 4), at which point the outflow tract has shifted to its definitive position, ventral to the right atrium (Manner, 2000). PAA III contributes to the brachiocephalic and common carotid arteries. The right lateral PAA IV contributes to the adult aortic arch. The left lateral PAA IV regresses. PAA VI contributes to the ductus arteriosus and parts of the central pulmonary arteries. Of the transitory arch pairs, PAA I and II remodel into capillary beds, whereas PAA V is fleetingly seen as a segment of PAA VI (Hiruma and Hirakow, 1995; Hiruma et al., 2002). This sequence of growth and remodeling is conserved across species, although in mammals, the dominant side is reversed, with the left lateral PAA IV contributing to the mature aortic arch and the right lateral PAA IV forming part of the subclavian artery. Perturbations to this programmed sequence of events, can lead to severe cardiac abnormalities.

In this present study, we have developed a novel imaging and multiscale computational model pipeline to quantify and analyze local, segment by segment, stage-specific and subject-specific PAA hemodynamic and morphological changes during a critical window of development at HH18, HH24 and HH26 (Fig. 1), looking at the natural variation that may present itself at a particular stage. WSS and pressure are quantified in the different subjects and across stages, along with area, length and other morphological parameters, to determine which drive growth. We perform for the first time in the PAAs, a group-based parallel numerical study, using detailed segmentations of stage-specific arch artery systems obtained from *in vivo* measurements. We offer a new way of analyzing morphogenesis through the lens of quantitative variability analysis. Ultimately, establishing norms for critical windows of development that take into account stage-specific variability will help identify the origins of congenital malformations and provide insights into the optimal timing for restorative interventions.

RESULTS
### Growth and remodeling of the early pharyngeal arch artery system
In order to assess hemodynamic-driven growth, both morphological and hemodynamic parameters must be thoroughly categorized

and a relationship between the two established. Characterizing morphological and hemodynamic growth patterns requires a method to track changes in PAA morphology and blood flow dynamics over a period of time. The more local the tracking, the less assumptions need to be made and the more variability can be analyzed. Our 'high-resolution imaging and flow measurement to multiscale numerical analysis pipeline' (Fig. 2) consists of two separate subject-specific numerical models obtained from 3D reconstructions of *in vivo* morphology. The 3D analysis allows for quantitative measurements of qualitative or previously unchecked observations. To create the pipeline inputs, embryos were open cultured and imaged via ultrasound. Pulsed-wave Doppler velocity curves were gathered for HH18, HH24 and HH26 embryos through B-mode guided videos. Small cohorts (*n*=5 per cohort) of embryos from each stage were perfusion fixed, stained with a potassium iodide and iodine solution and imaged by way of 3-4 μm voxel nano-CT scans. Resulting high-resolution image stacks were reconstructed and used as a basis for the numerical models. Doppler curves were then used as inputs into computational fluid dynamic (CFD) models to map out flow dynamics along the PAA manifold. The mapping of flow dynamics is important as blood flow and its resulting forces induce regional changes on the cellular and molecular level that are important for vascular morphogenesis. To make use of the detailed geometrical and hemodynamic parameters along the arch arteries of the 3D models, each arch was divided into ten equally spaced individual sections. This was achieved by establishing centerlines and perpendicular cross-sections along arch arteries and calculating desired parameters at each point. The division of arch arteries into segments allowed for the tracking of local growth within groups and across stages by enabling the comparison of growth between relative positions across multiple sources.

From the first high-resolution 3D numerical model, a second zero-dimensional (0D) circuit model of the vascular network was created. The model is considered 0D as the geometrical parameters such as area and length do not factor into the governing equations, but rather resistance is calculated based on the equation:

$$P_{in} - P_{out} = Q \times R, \tag{1}$$

where R is resistance, P_{in} represents the pressure at the beginning of a vessel, P_{out} the pressure at the end of the vessel and Q the
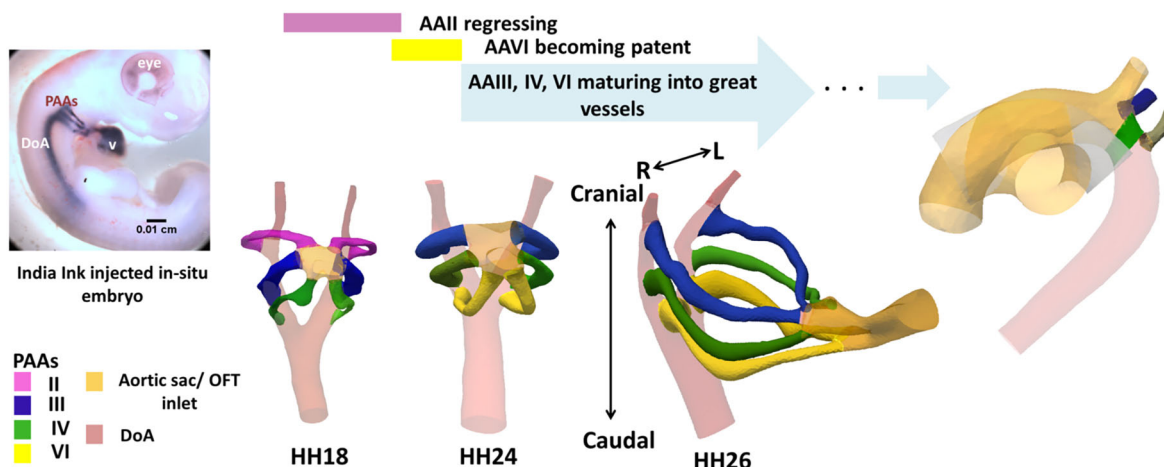
Fig. 1. Anatomical landmark figure of three stages considered in the current study. Summary of arches present per stage and changes taking place, as well as the final mature configuration. 3D arch manifolds are not shown to scale in order to facilitate readability. v, ventricle.
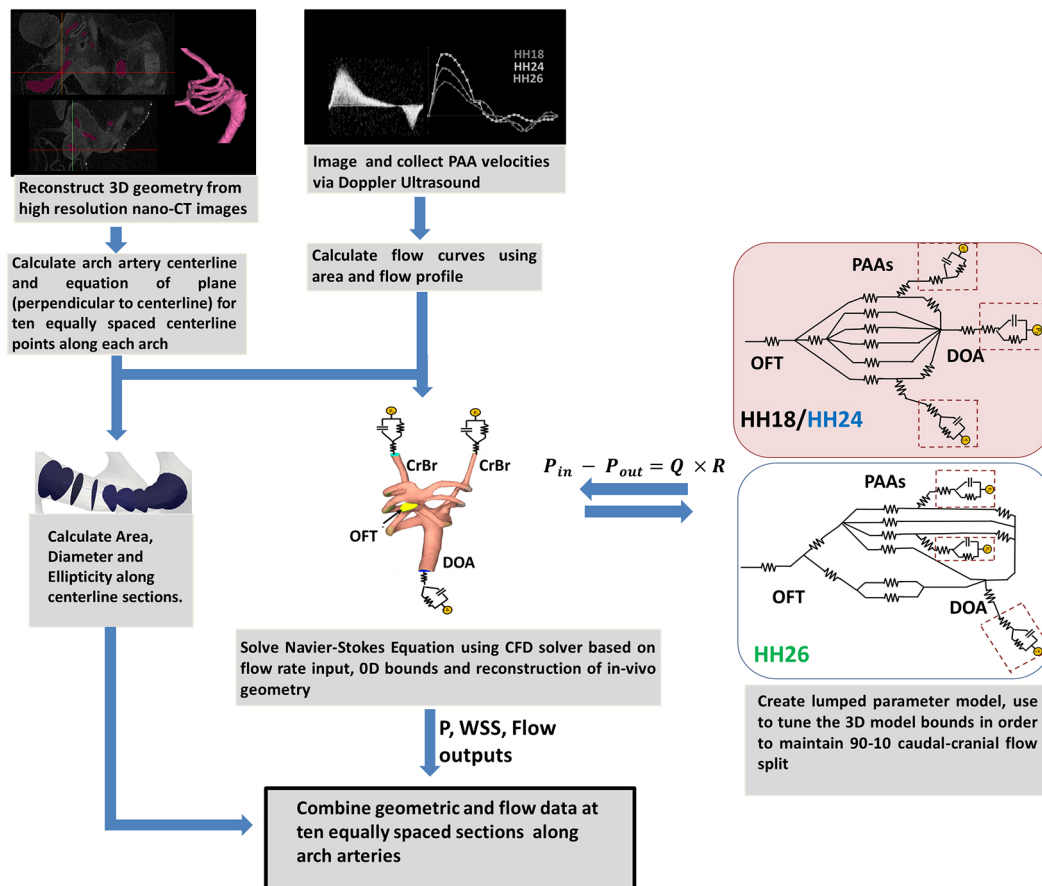
Fig. 2. High-resolution imaging and flow measurement to multiscale numerical analysis pipeline. B-mode guided-ultrasound velocities were gathered for embryos staged at HH18, HH24 and HH26. A selection of these embryos were perfusion fixed and imaged via (3-4 μm) nano-CT scans. 3D reconstructions of PAA morphology were obtained from these scans from which geometric data could be gathered directly. Centerlines were calculated for each vessel and perpendicular sections taken along the centerline. A Navier–Stokes CFD solver was used to obtain pressure, WSS and vessel-specific flow data in the 3D geometry. From the 3D simulation, 0D models were created using pressure drop and average flow per vessel (see Fig. S4 for a more detailed 0D model view). Hemodynamic and geometrical information were combined by using the same sections along the centerline (ten per arch) to record hemodynamic parameters.

average flow through the vessel. This second 0D model served as both a means of further analysis, as it enabled quantification of the overall effect that arch artery characteristics had on flow, and served as physiologically relevant bounds for the 3D numerical simulations (see Materials and Methods for further explanation).

Morphological changes measured from 3D reconstruction
PAA evolution was first evaluated from HH18 to HH24, as it marks a critical remodeling period, notably the growing in of PAA IV, the primitive segment of the aortic arch, and the regression of PAA II into capillary beds. From HH18 to HH24, the outflow tract (OFT) itself shifts in position, moving ventral to the right atrium, and loses its once tubular character by HH24 (Manner, 2000). The embryo is rapidly growing and must account for a 108% change in blood volume (Rychter et al., 1955). In order for the PAAs to accommodate a larger blood volume, the arch arteries themselves must grow in length, diameter or cross-sectional area (CSA). Detailing these changes, allows us to understand how this growth comes about. Through the 3D reconstructions of *in vivo* morphology, calculation of curved arch length taken along the arch artery centerline was possible (Fig. 3). At HH18, PAA II, which will dissolve into capillary beds, is by far the longest arch, at 0.17±0.04 cm (right) and 0.17±0.03 cm (left), longer than its HH24 PAA III and IV (right and left) cranial counterparts and just under

the PAA VIR and VIL (VI right and left, respectively) counterparts at HH24. The 3D reconstructions also revealed stage-specific shape and CSA changes along the arch arteries (Fig. 3A,B). Among HH18 embryos, vessel CSA are elongated along the horizontal (R↔L, Fig. 1) axis. By HH24, arch artery cross-sections become more round and less elongated in the horizontal direction. Centerline calculations allowed for evaluation of the way vessels branch off the aortic sac and its evolution over time. The angle at which a vessel branches off its parent vessel influences the immediate flow properties of the fluid moving through the conduits (Sinibaldi and Romano, 2017). This angle also dictates the amount of force (in the form of pressure) necessary for flow to change direction and embark on a new fluid path. In general, a smaller angle favors fewer secondary flows and requires a smaller pressure gradient to drive the flow through the junction. A branch-splitting angle (Fung, 1997) was calculated for each of the six arch arteries based upon the centerlines of the vessel of origin and the centerline of the new branch. Fig. 3D displays the branch splitting angles for the split of the DoA into a left and right branch, as well as well as the OFT inlet split into the six PAA vessels. For PAA III and VI (right and left), the branch splitting angle decreases with growth, whereas the angle of PAA IV (right and left) increases from HH18 to HH24. The angle can be thought of as the spreading or initial spacing between the vessels in the cranial caudal direction. As the vessels mature, they
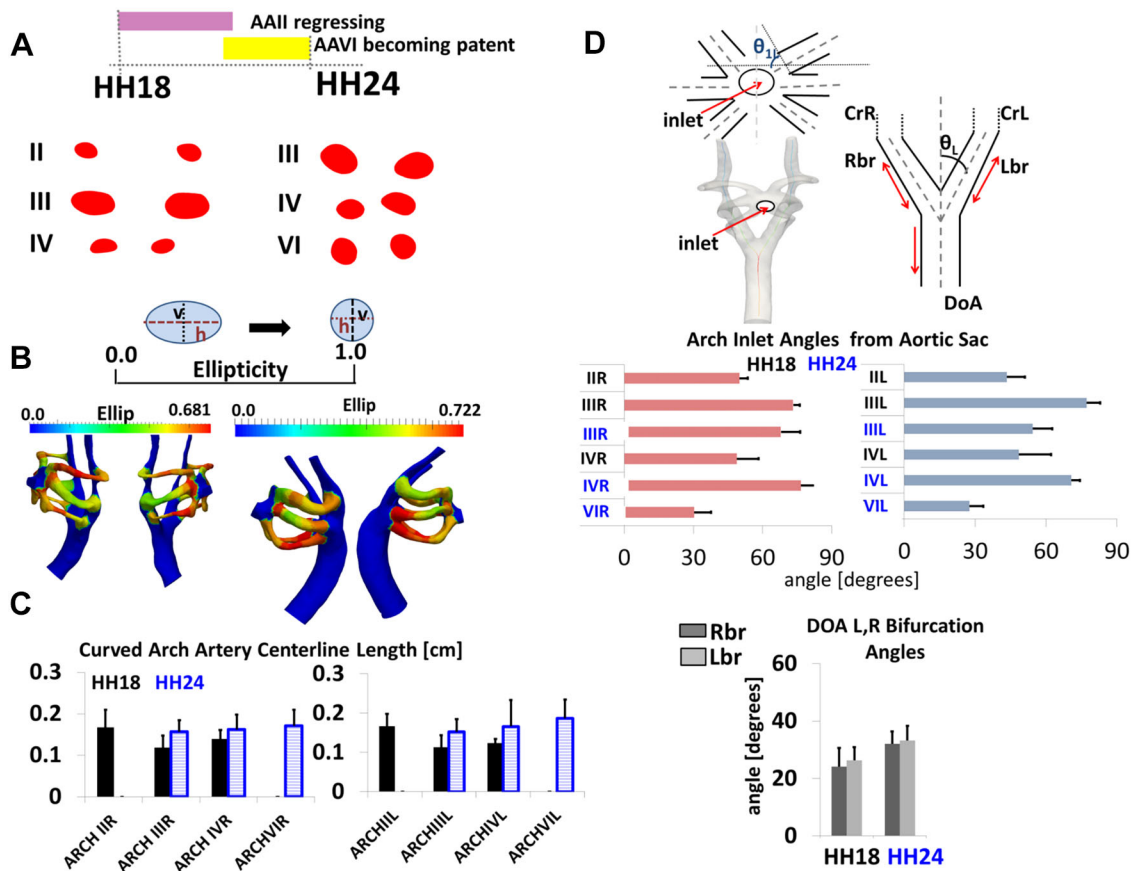
Fig. 3. HH18 to HH24 morphological changes measured from 3D reconstructions. Ellipticity represents the ratio of the minimum vessel diameter to the maximum vessel diameter, with an ellipticity of 1 indicating a perfect circle. (A) Vessel cross-sections, highlighting the shape changes. (B) Mean geometrical models for each stage with the corresponding ellipticity values for ten cross-sections mapped on the surface of each arch. (C) PAA length per arch (±s.d.). (D) Branch-splitting angles are displayed in degrees for arch inlet angles and DoA outlet angles (±s.e.m.). For inlet angles, a bisector was taken for the aortic sac, a perpendicular was dropped to this bisector and the angle where the perpendicular of the bisector meets the centreline was taken to be the branch-splitting angle. For the DoA, the centreline of a single dorsal tube was extended and the angle was measured between the extension and respective branch centreline. No significant changes were found for HH18 to HH24 length or angle changes when compared considering a two-tailed paired *t*-test. Cr, cranial branch (right and left). *n*=5 embryos per stage; *P*<0.05 for significance.

become more parallel, more in-line with each other and closer together, rather than splayed in the cranial-caudal direction. DoA branch splitting increases between HH18 and HH24. The left branch angle remains slightly more elevated than the right branch angle.

Hemodynamic and geometric changes measured from 3D reconstruction

Fluid dynamic parameters are ultimately dependent on flow velocity and flow distribution throughout the arteries. To understand how flow dynamics shift throughout development, we examined changes in flow distribution over time/stages (Fig. 4) through the 3D numerical simulation. For HH18, the right and left third arch consistently receive the largest amount of flow in the developing HH18 embryo, receiving between 79% and 92% of flow through the arches over the course of one cardiac cycle. The right side receives more flow in two of the five HH18 embryos, whereas the left side received an average of 15% more flow in the three other cases (Table S1A). Within the HH24 cohort, the embryo obtains a more balanced flow distribution across the arches. Rather than one arch pair uniformly receiving upwards of 73% of the flow, HH24 embryos have an average of 42% (±12.9%), 39.3% (±4.1%) and 18.5% (±13.2%) mean flow distribution across the arch pairs (III, IV

and VI, respectively). In HH24 embryos, the right fourth arch receives over 25% of the flow in three out of five embryos (Table S1B). Surprisingly, the left fourth arch received over 25% of the flow in the remaining two embryos and flow dominance was shifted to the left side in these embryos. When comparing arch pairs across stages, relative standard deviation (RSD) (standard deviation normalized to the mean value) stands at 62.9%, 6.2% and 35.7% for HH18 PAA II, III and IV pairs, respectively, and at 30.5%, 10.4% and 73% for HH24 PAA III, IV and VI pairs. These data suggest that more-malleable HH18 II and IV arches, in terms of flow distribution, permit a more controlled PAA III pair, whereas more malleable HH24 III and VI arch pairs permit a more controlled PAA IV pair.
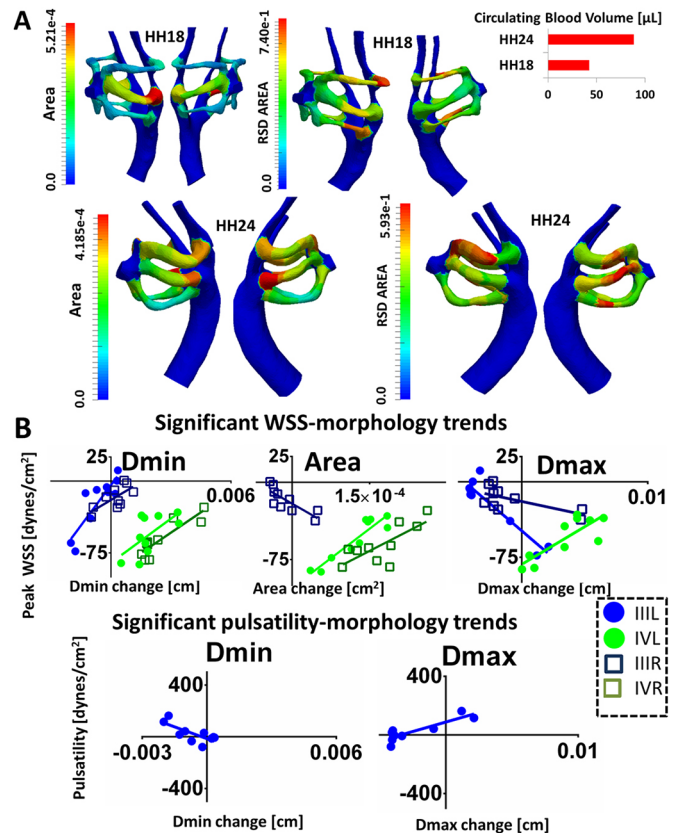
Hemodynamic-driven (or mediated) growth could arise from two different mechanisms. Transmural pressure or WSS could lead to increases or decreases in vessel area or diameter. Using the 3D numerical simulation, we were able to analyze pressure and WSS values across PAAs (Fig. S1). HH18 peak pressure values vary across the cohort of five (Fig. S1A), but pressure patterns remain consistent: a peak that originates in the OFT inlet and dissipates cranially up the aortic sac and laterally through the arches, with the most caudal arch pair (IVR and IVL) absorbing the highest pressure per arch length (Fig. 4B). Peak pressure varies between
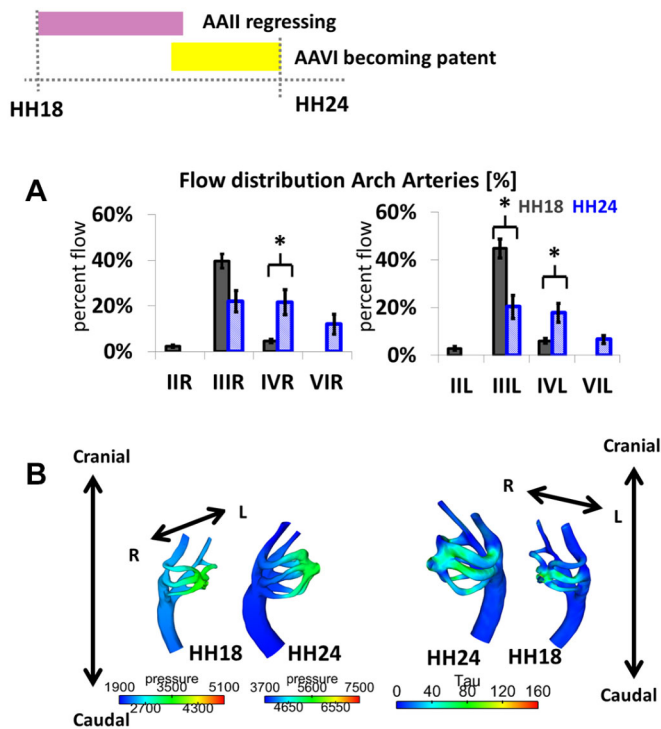
Fig. 4. HH18 to HH24 hemodynamic changes measured from 3D numerical simulations. (A) Flow distribution per arch (±s.e.m.), asterisks indicate significant changes (n=5 embryos per stage; *P<0.05, two-tailed paired t-test). (B) Pressure and WSS (dyne cm^{-2}) at peak flow for a representative HH18 and HH24 embryo, full cohorts are displayed in Fig. S1 in the supplementary information. Though the magnitude of the pressure changes from stage to stage, it is greatest at the inlet and through the aortic sac, before being dissipated through the arches. Peaks in WSS can be found at the inlet junction and large PAA III for HH18 embryos, and at the inlet junction and several arches for HH24 embryos.

Fig. 5. Hemodynamic-driven geometric changes. (A) Mean geometrical models for each stage with the corresponding CSA values for ten cross-sections mapped on the surface of each arch, along with their RSD (s.d. normalized to the mean at that point). (B) Linear regressions were plotted to highlight correlations between hemodynamic forces and area diameter changes, peak WSS-driven vascular growth trends and pulsatility-driven trends. Axes show change in x and y values. Only significant trends are shown. The circulating blood volume legend is adapted from Rychter et al. (1955), and is intended to keep in perspective the large amount of changes in terms of flow volume the embryo is undergoing across stages. n=5 embryos per stage; P<0.05 for significance. D_{min}, minimum diameter; D_{max}, maximum diameter.

5100 dyne cm^{-2} (3.83 mmHg) and 2900 dyne cm^{-2} (2.17 mmHg) at peak flow (Fig. 4B), with an average arch pressure of 3387 (±128) dyne cm^{-2}. HH24 embryos mark a rapid increase in pressure, but conserve the same pressure dissipation pattern, with the most caudal arch pair absorbing the largest amount of pressure per arch length (PAA VIR and VIL) (Fig. S1B). HH24 pressure magnitude varies between 7500 dyne cm^{-2} (5.63 mmHg) and 4650 dyne cm^{-2} (3.49 mmHg) at peak flow (Fig. 4B). Average arch pressure increases to 6072 (±389) dyne cm^{-2}, an increase of 79% from the HH18 cohort. HH18 peak WSS is 48.15 (±23.59) dyne cm^{-2} across embryos. Spikes in WSS can be seen at the inlet in the aortic sac near the third PAA entrance, as well as laterally along the length of the arch (Fig. 4B, Fig. S1D). HH24 embryos exhibit an increase in spatial frequency of WSS spikes with a per arch WSS magnitude of 94.74 (±5.58 dyne cm^{-2}) at peak flow (Fig. 4B, Fig. S1E). Although the per arch magnitude of WSS greatly increased, HH24 WSS magnitude remains on the same scale as that of HH18 embryos.

To distinguish between pressure and WSS as drivers of PAA remodeling, we quantified morphology changes from CFD-aided 3D models using data obtained from the point-to-point segment markers (n=5 embryos per stage, 10 markers per arch, 6 arches per embryo). Statistically significant changes between the relative position at HH18 to the relative position at HH24 were found through linear regression of data obtained per arch (Fig. 5, Table S2). Variations within each stage are shown in the form of RSD (Fig. 5A). HH18 to HH24 change in peak WSS magnitude leads to

significant arch artery correlations for PAAs IIIL, IIIR, IVR and IVL (Fig. 5B). The majority of these changes were associated with positive slopes, 30% were associated with a negative slope (Fig. 5B; Table S2). Because flow through these arches assumes a parabolic or Poiseuille flow profile, we can determine which factor (morphological or hemodynamic) drives such slope changes. As Poiseuille WSS magnitude is proportional to flow over radius cubed (Q/r^3) or equivalently mean velocity over radius (v_{mean}/r), a positive slope suggests that change in flow or mean velocity are locally driving growth in the arches at these stages, whereas a negative slope implies the geometric feature (D_{max}, D_{min}, Area) is dominating the local growth between stages over flow or mean velocity. This analysis revealed that WSS played a significant role in promoting growth between stages, with WSS driving growth in IVL area changes, and PAA IIIL and IVR minimum diameter changes (Table S2). The same technique of quantifying a relationship between hemodynamic and geometrical changes was used for pressure in the form of pulsatility (difference between maximum and minimum pressure over a cardiac cycle). Pulsatility correlates with diameter changes in the early arch arteries (Fig. 5B). For HH18 to HH24 growth, significant trends were found for PAA IIIL. D_{max} was associated with a positive

slope, whereas D_{min} was associated with a negative slope. Pulsatility can be considered a secondary driver of growth in HH18 to HH24 remodeling.

Understanding growth through variability: a major period of transformation

One of the strengths of the current technique is the ability to examine the changes in an individual (subject-specific configuration), and to highlight and learn from the changes in configurations that are at the same stage. Rather than assessing an overall general trend based on idealized composite geometries, this new technique allows for local as well as global variability analysis and therefore fosters an understanding of multiple forms of healthy development and how the progression comes about. Thus, as a first application of this technique, we examined the variations in HH26 embryos. Because of the major changes taking place in HH26 embryos, there is a larger bell curve of variation (Fig. S2), that convey a story of PAA growth and remodeling. These embryo to embryo variations in PAA geometry are especially pronounced during major transition phases where multiple configurations may be present at the same HH stage (Kowalski et al., 2013). Despite identical wing and limb bud characteristics, statistically significant differences were found for CSA and ellipticity parameters among subsets. HH26 marks a major time point of change, as cardiac septation or partitioning of the heart has begun. The aorticopulmonary septum has lengthened toward the heart and entered the distal OFT (Waldo et al., 1998), separating the OFT into an upper and lower section due to protruding mesenchyme right before the entrance to the PAAs. The large lengthening of the aorta and pulmonary trunk are reflected in Fig. 6C. Differences in timing

and/or rate of lengthening, rotation and septation of the arches resulted in HH26 subsets that we refer to as 'slow' and 'fast' (Fig. 6A). The three configurations present at this stage allow for a better understanding of how the vessels evolve and the effect of OFT septation on the arches themselves. PAA cross-sections continue to become more round through HH26, obtaining an almost perfect circular cross-section at HH26-slow (Fig. 6A,B blue) before elongating in the vertical (cranial-caudal) direction (Fig. 6A,B red). HH26-fast embryos still feature this characteristic elongation in the vertical direction (Fig. 6B green). HH26-fast embryos exhibit more elliptical (particularly in the latter half) intricate arches with smaller CSAs when compared with the HH26 subset.

Owing to morphological changes in how arches connect to OFT (Fig. S4), flow is no longer required to mount the aortic sac in order to distribute to the more cranial arches as it was with the previous stages. The average flow distribution between arch pairs is 25% to 21% to 55% for PAA III to PAA IV to PAA VI arch pairs. The right and left sixth arches begin to receive the majority of flow, between 55% and 72% of the flow in four of the five HH26 embryos, and 25% of the flow in the less developed HH26-slow embryo. Pressure continues to increase substantially from HH24 to HH26. Across the HH26 embryos, peak pressure varies between 9350 dyne cm^{-2} (7 mmHg) and 15,000 dyne cm^{-2} (11.25 mmHg) at peak inlet flow (Fig. 7A), double that of the HH24 embryos. Despite the large increase in overall pressure magnitude, average pressure per arch, 6964 dyne cm^{-2} (±214), is up only 15% from HH24 embryos, highlighting both the substantial increase in PAA length and the power of the septated OFT inlet to dissipate pressure. The caudal most arch pair (here, arch VI R and L) no longer consistently bears the largest pressure magnitude per arch length. In general, pressure
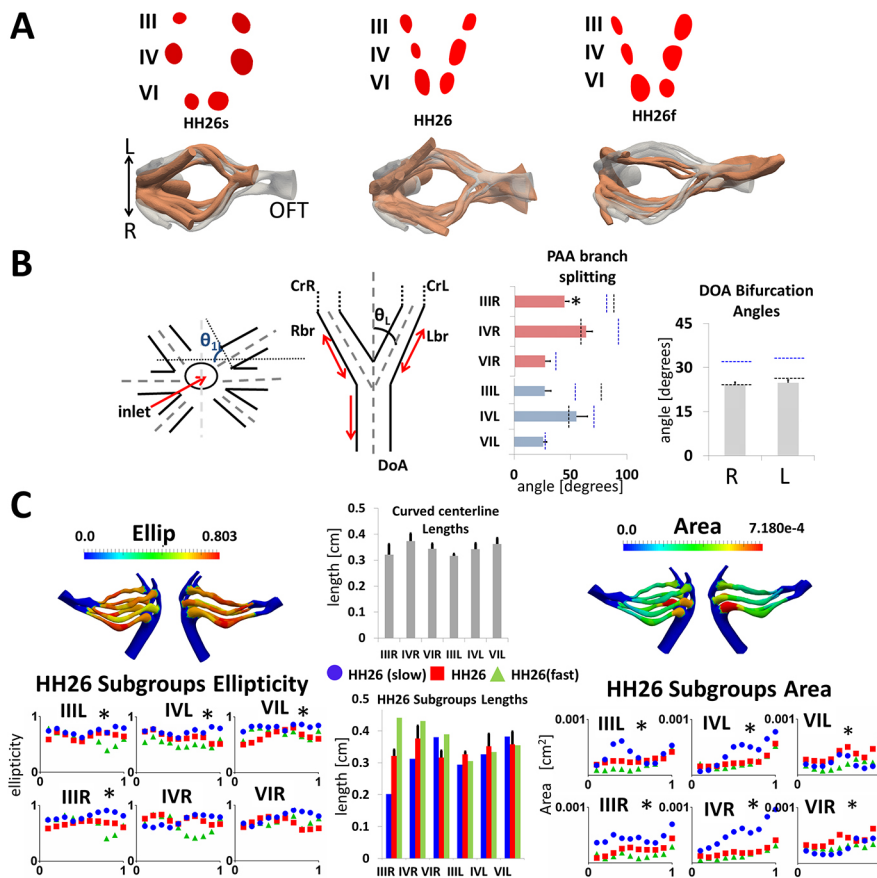
Fig. 6. HH26 morphological changes measured from 3D reconstructions. (A) Vessel cross-sections, highlighting the shape changes that exist across HH26 subsets. A top down view of a PAA manifold is shown beneath with gray showing the mean HH26 mean template and flesh-colored geometries showing subset geometries. (B) HH26 branch-splitting angle (±s.e.m.) with mean values for HH24 (blue) and HH18 (black) displayed as dashed lines along corresponding arches. All angles decrease from HH24 onwards. *P<0.05 compared with HH24 branch-splitting angle (IIIR). (C) HH26 mean values for ellipticity, curved centerline lengths (±s.d.) and area (cm^2) with a subgroup breakdown shown for each of the three parameters. All HH26 PAAs were significantly longer than HH24 embryos (two-tailed paired t-test). The breakdown of HH26 subgroup ellipticity along the arch shows that HH26-slow consistently displays the most circular cross-sections along the arch (with the exception of the first one-third of PAA IVR and one-fifth of PAA VIR), whereas HH26 and HH26-fast embryos are frequently as skewed as HH18 embryos (average ellipticity ~0.6), particularly in the latter half of the arch. Similarly, a breakdown of area along the arch by subgroup shows how HH26 area is generally larger than HH26 and HH26-fast embryos along the arch and HH26-fast possess the smallest CSA along the length of the arch. Although significant changes were not found in overall arch lengths between subgroups, ellipticity subgroups were found to be significantly different for all arches (apart from IVR and VIR) and area was found to be significant across groups. *P<0.05, Friedman test, n=5 embryos (HH26).
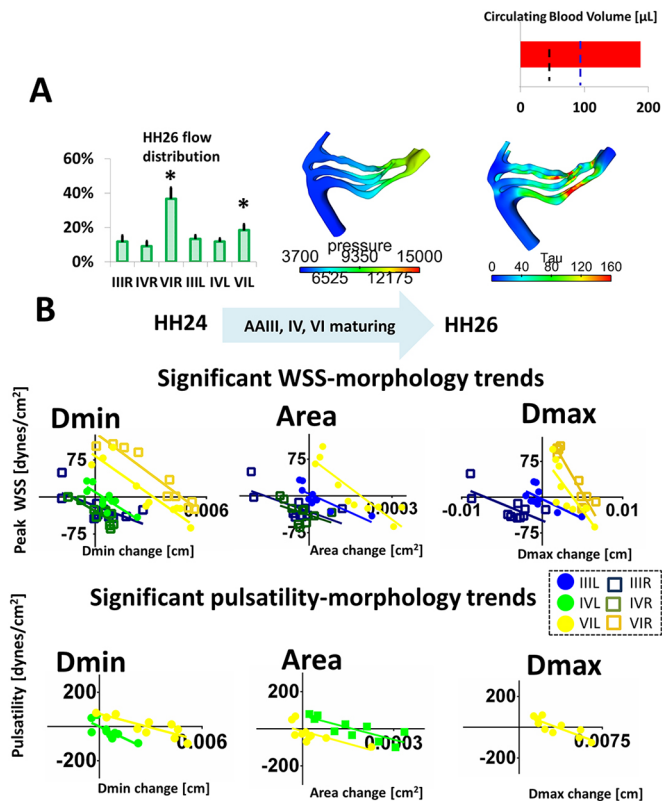
Fig. 7. HH26 hemodynamics. (A) Flow distribution (±s.e.m.), pressure and WSS (dyne·cm^{-2}) for HH26 embryos. (B) Linear regressions were plotted to highlight correlations between hemodynamic forces and area diameter changes, peak WSS-driven vascular growth trends and pulsatility-driven trends. Axes show change in x and y values. Only significant trends are shown. The circulating blood volume legend is adapted from Rychter et al. (1955), dashed lines refer to HH18 circulating blood volume (black) and HH24 circulating blood volume (blue). D$_{min}$, minimum diameter; D$_{max}$, maximum diameter.

is dissipated almost equally along OFT junctions and dissipates in a uniform fashion along the bilaterally paired PAAs. Pressure is distributed least uniformly in the HH26-slow embryo (HH26-5, Fig. S1C), where the L caudal VI arch still receives the largest pressure load, as with its HH24 counterparts. WSS levels remain at the same magnitude as those of HH18 and HH24 embryos, with overall WSS per arch magnitude of 91.48 (±21.56) dyne cm^{-2}, a slight decrease from HH24 embryos. Given these CFD obtained pressure, WSS and flow values, we again sought to determine whether WSS continued to drive these changes and whether pulsatility was a secondary driver. We performed linear regressions on HH24 to HH26 change in hemodynamic and change in morphological parameter data. As cardiac septation is a major programmed event, we hypothesized that the morphological changes would lead to the necessary hemodynamic changes. For peak WSS, significant correlations were found for PAA IIIR, IVR, IVL, VIL and VIR. As hypothesized, slopes for all HH24 to HH26 growth were negative, indicating that the geometric feature is dominating the local growth between stages over flow or mean velocity (Fig. 7B). Pulsatility maintains its role as a secondary driver of PAA growth with significant trends found for PAA IVL and VIL. Through the HH26 subsets, we see how the 'lengthening and rotation of the aorticopulmonary septum toward the heart' translates to a simultaneous pulling of the arch arteries from their OFT inlet and stretching along the cranial dorsal axis. These movements

render the PAA cross-sectional areas more circular and then oval in the cranial-caudal direction, and work to maintain shear stress levels, while distributing the mounting pressure in a more uniform fashion. The effect of ellipticity on hemodynamic parameters is further detailed in Fig. S3.

Validation of computational hemodynamic parameters

To validate hemodynamic outputs from the computational simulations, in silico flow measurements and flow distribution of the PAA network were compared with experimental measurements (Fig. 8). At the level of the DoA, HH18 and HH24 flow curves are compared with those of Yoshigi et al. (2000), while HH26 average flow is compared with that of Hu and Clark (1989) (straight lines). Ultrasound velocities (Fig. 10) were converted into flow curves based on average PAA area along the arch and on Poiseuille or plug flow assumptions for the spatial profile. In general, there is a good agreement between computational and experimentally obtained values, with a significant difference between in vivo- and in silico-derived arch flow splits existing only for arch IIR based off a two-tailed Mann–Whitney U-test. When comparing in vivo and in silico flow splits across all arches, no significant changes are found for any of the present stages (two-tailed Mann–Whitney U-test). Although flow distribution hierarchy in terms of which arch received the most and the least amount of flow was consistently conserved between experimental and computational measurements, HH18 IIR and IIL flow was more constrained in silico than in vivo. Nevertheless, these comparisons indicate that in silico approximations of in vivo conditions are reasonable. Pressure waveforms were not measured or used as a direct input for boundary conditions in 3D simulations; rather, these values were indirectly controlled through the 0D bounds. Values are consistent with literature values measured at the level of the DoA by Yoshigi et al. (2000) and Zahka et al. (1989).

Growth across stages: interplay of hemodynamics and morphology

In an effort to understand the physical transformation occurring between stages, rather than change in stage to stage end points, statistical shape modeling was used to transform HH18 (using only the persistent arches, and not the regressing PAA II pair) to HH24 (without the growing PAA VI pair), and then HH24 (all 3 arch pairs) to HH26 (Fig. 9A). Statistical shape modeling (Deformetrica; Durrleman et al., 2014) was chosen as it handles complex amorphous structures and creates an unbiased indication of the most likely path of morphogenesis if overall distance minimization between shape distributions was the controlling variable (see Materials and Methods). Although the transformed geometries are not identical to the mean average geometry (template) at the transformed stage, understanding what displacement fields are necessary for embryos to approach the template shape leads to a better understanding of the changes taking place. HH18 to HH24 surface area displacement is highest in the cranial DoA branches and the ventral half of PAA IV. These patterns differ greatly from both the pressure and WSS HH24 maps (Fig. 4B). The magnitude of HH24 to HH26 3D surface displacement is more than double that of HH18 to HH24 deformation, consistent with the doubling of both the change in circulating blood volume (Fig. 7, top) and the change in pressure magnitude from HH24 to HH26. The HH26 displacement field resembles that of HH26 pressure maps (Fig. 7A), with displacement highest at the OFT inlet and dissipating through the arches toward the DoA. High displacement values also appear in the right cranial arch and the caudal-most section of the DoA on the transformed HH26 embryo. Although pressure (in the form of
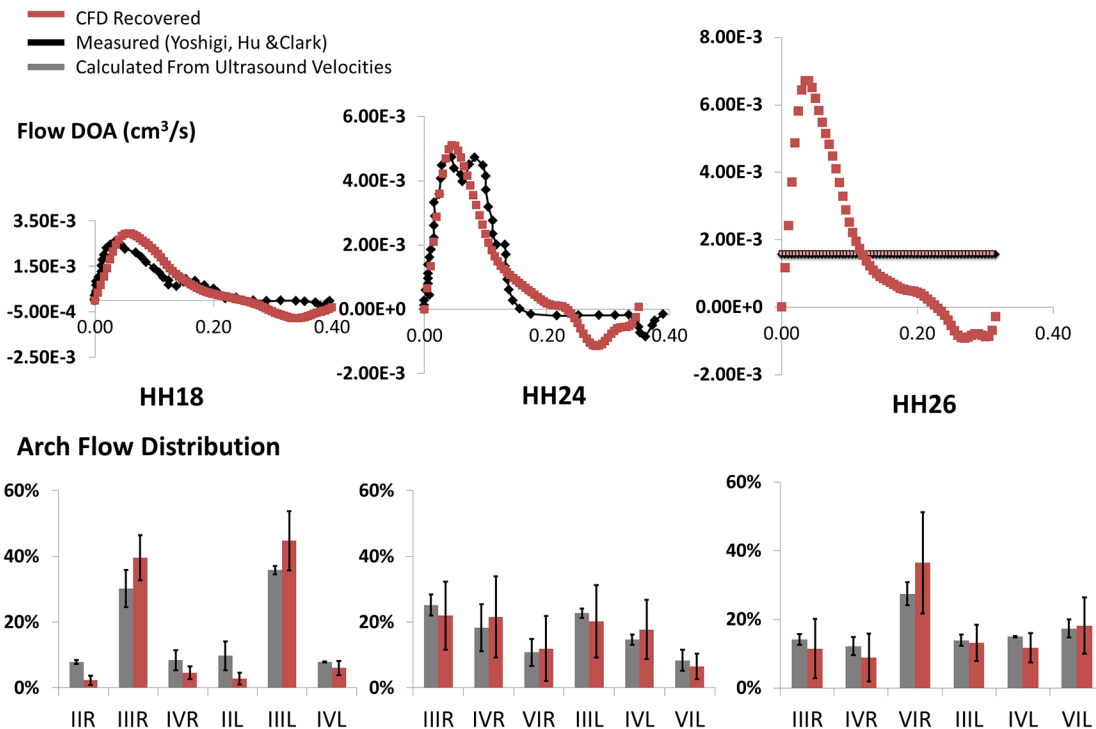
Fig. 8. Computational fluid dynamics validation with experimental measurements. Pulsatile flowrate profiles over one cardiac cycle computed at the DoA compared with experimental values taken with a flow meter, as well as *in silico* PAA flow distribution compared with Doppler computed arch flow distribution. HH26 embryos are compared with the average flowrate (straight line) as full DoA flow profiles were not available. Error bars represent s.d. $n=5$ embryos per stage *in silico*; $n=8$ (HH18), $n=11$ (HH24) and $n=14$ (HH26) *in vivo*; *$P<0.05$ for significance, two-tailed Mann–Whitney.

pulsatility) only played a small role in local diameter and area changes, pressure magnitude may play a larger role in overall arch movement and elongation from HH24 to HH26.

The second numerical model, which breaks down the PAA morphology into electrical analogs, offers another concrete way of examining growth by quantifying ease of flow transport through a vessel. From a flow perspective, each vessel or flow conduit, including the aortic sac, can be summarized through a single resistance value. The higher the resistance, the harder it is for flow to travel through and the more force is needed to ensure continuous circulation. To summarize how the system as a whole changed, resistance values for PAA manifolds were combined into a single resistance value per embryo, called the equivalent resistance (R_{eq}). There is a 7% increase between R_{eq} values for HH18 and HH24 embryos. A 106% increase exists between HH24 and HH26 R_{eq} values. Coupled with the displacement field metrics (Fig. 9A), the R_{eq} increases underscore the effects of vessel morphology on the functionality of the PAA system. On an individual arch artery resistance level, the general trend is a decrease in resistance values between HH18 and HH24 followed by a general increase in resistance values between HH24 and HH26. Statistically relevant changes exist only between HH18 and HH24 arch IVLs ($P=0.035$) and between HH24 and HH26 arch VIRs ($P=0.045$). When displayed in the context of a resistance versus area graph (Fig. 9C), regression, growth and maturation trends are consistent with generally accepted ideas of vascular growth, particularly as it relates to length and CSA changes (Fig. 9). The regressing PAA IIR and PAA IIL have the highest resistance and smallest mean CSA. HH18 PAA IVL and HH24 PAA VIL have almost identical resistance area values. These caudal arches are both growing in on their respective stages. For the established arches (PAA IIIR and PAA IIIL), HH24 resistance values increase from HH18 to HH24,

consistent with the narrowing of the vessel diameters and decrease in CSA. The decrease in resistance value for maturing vessels is consistent with Poiseuille estimated resistance (1/Area^2 or equivalently 1/Radius^4). Similarly, elongation that corresponds to an increase in length and decrease in area is associated with an increase in resistance. Resistance-area arch trends across stages (Fig. 9C) are fitted by an exponential function ($R^2=0.66$). WSS versus surface area arch-specific values (Fig. 9C) resemble that of a third order polynomial (R^2 value=0.56), and indicate size-specific sensitivity zones for WSS-driven surface area changes. WSS-surface area graphs again underscore WSS maintenance of a 20-160 dyne cm^{-2} range. Percent flow versus volume change graphs (Fig. 9C) highlight the evening out of the HH26 cranial most arches (flow percentage values, *y*-axis) and extreme increase in robustness/volume of the caudal 'trunks' (volume change values, *x*-axis). Percent flow-volume change graphs also emphasize how hemodynamic and morphological characteristics from one stage promote changes in the subsequent stage. These trends are consistent with information obtained from hemodynamic-morphology graphs (Figs 5 and 7). If hemodynamics were found to lead growth of a particular PAA from one stage to another, a small percentage flow value will lead to a small volume change (e.g. HH18 PAA IVR, IVL). If morphology were found to lead growth, a small percentage flow value may be associated with a large volume change (e.g. HH24 PAA VIR, VIL).

In order to determine which areas along the arch were the most tightly controlled in terms of hemodynamic and morphological parameters, we examined relative variability of pressure and WSS in conjunction with relative variability of D_{min}, Area and D_{max}. This local tracking is important, as regional differences in mechanical force, rather than overall levels, promote vascular remodeling. As morphological changes sometime lead hemodynamic changes,

DEVELOPMENT

8
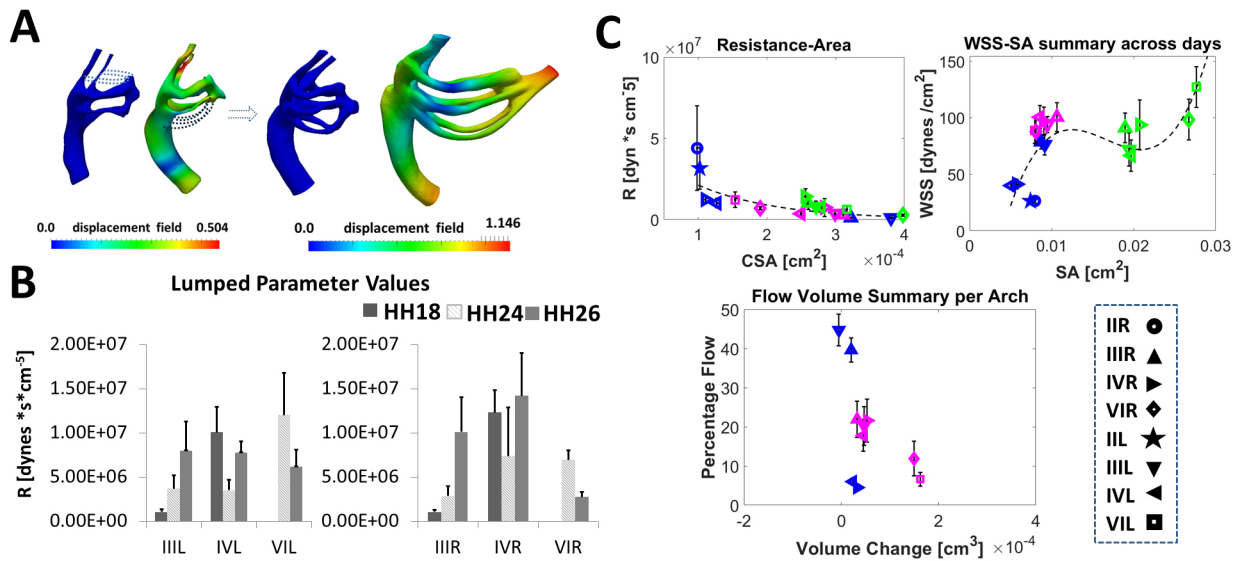
Fig. 9. Cohort-based PAA growth and remodeling dynamics. (A) Statistical shape modeling-based HH18 to HH24 growth (in cm) (dashed lines indicate a regressing or appearing arch not included in statistical shape modeling) and HH24 to HH26 growth. (B) 0D resistance values for each arch per stage. (C) Single-value hemodynamic versus geometric parameter graphs for major flow drivers (resistance area, WSS surface area and flow distribution volume graphs). Percent flow-volume graphs show the previous stage percentage flow with the following stage change in volume value. Resistance versus area and WSS versus surface area show current x values with current y values. Standard error bars are shown in black.

and vice versa, highlighting combined least-variability areas may help identify regional promotors of change. Deviation from mean was calculated for all arch sections among all embryos (ten sections per arch, five embryos per stage) (Fig. S5). Mean deviation was taken to be the difference between the mean and specific value normalized to the mean. The least variable region, from a combined hemodynamic-geometric perspective, was determined for each category (P-D_{min}, P-Area, P-D_{max}, WSS-D_{min}, WSS-Area, WSS-D_{max}) and each stage (HH18, HH24, HH26) (Table 1). The least variable regions for HH18 embryos were sections 1 and 2 along the arch, whereas the least variable regions for HH24 and HH26 embryos were in the latter half of the arch, particularly section 10. Surprisingly, trends did not always correlate with significant WSS- and P-driven area diameter changes, as determined through linear regression (Figs 4B, 6B, ST2). For example, WSS was found to be a major driver of HH18-HH24 Area IVL trends ($P<0.0001$, $R^2=0.86$), but the least variable WSS-Area regions are found along PAA IIIL for both HH18 and HH24 embryos. Conversely, WSS was found to be a major driver of HH18 to HH24 PAA IIIL D_{min} changes ($P=0.001$, $R^2=0.76$), and the least variable HH18 and HH24 WSS-D_{min} regions are found along this arch, as well as the least variable HH24 P-D_{min} region. We believe the highlighted regions should be closely watched when determining whether development is proceeding in a healthy manner. These regions should also be examined at the cellular/molecular level to determine whether their composition is the same as the surrounding vessels; they may serve as markers of normal development.

DISCUSSION

The dissemination of comprehensive three-dimensional atlases of development can serve as a powerful reference (de Bakker et al., 2016; Rana et al., 2014). More powerful still is the establishment of a range of healthy in addition to general trends for 3D morphogenesis. Examining variability to understand spatiotemporal morphogenetic and hemodynamic tolerance ranges, can help identify growth/adaptation mechanisms, determine risk corridors for malformation

and predict locations of primary causation. RSD templates, like the one shown in Fig. 5A, help to identify which areas along the arch are more conserved and where high zones of variation ('hotspots', orange/red) exist. In HH18 embryos, the positions along the arch with the largest variation exists both along the IVL arch, in keeping with the fact that this vessel is growing inwards, and the regressing PAA IIL. With the growing in of PAA IVR, the highest relative variation exists along the center segment of the arch, suggesting an outward growth from the connections at either end. The beginning and end arch segments are also the most tightly controlled on a geometric-hemodynamic variability level (Table 1). As PAA IV (right and left) grows in, the vessel is narrowest through its midpoint section (Lindsey et al., 2015). The same is seen for PAA VI. As these vessels mature, the center segments obtain comparable area-diameter values with that of the rest of the vessel. Vessel regression follows an opposite trend, with apoptosis and reduction in vessel lumen diameter beginning at the midpoint before the proximal and distal ends disappear (Molin et al., 2002). HH24 embryos show the largest variation on right side vessel midpoints, as well as the first half of PAA IIIL. From HH18 to HH24, flow is shifting from flowing primarily through arch pair III to a more even flow distribution. The largest relative area variation for HH26 embryos takes place at the PAA IVR midpoint. By this time, the vessels have been separated into an ascending aorta and pulmonary trunk, with the most caudal VI arch pair receiving the majority of the flow and PAA IVR receiving the least amount of flow. Section 1 of PAA IVR has the least variable HH26 WSS-D_{max} zone, consistent with systematic flow percentage reduction to this arch.

WSS maintained a central role in PAA growth. The relatively constant magnitude of WSS across stages (20-160 dyne cm^{-2}) suggests that this is a value to be maintained, in keeping with known trends (Beloussov, 2008; Taber, 2009). Linear regressions revealed a total of ten trends for HH18 to HH24 growth, and 13 trends for HH24 to HH26 growth. Twelve of these trends regulated growth on the right side while 11 of these regulated growth on the left side (Table S2, top). In addition to trends within arches, when reduced to
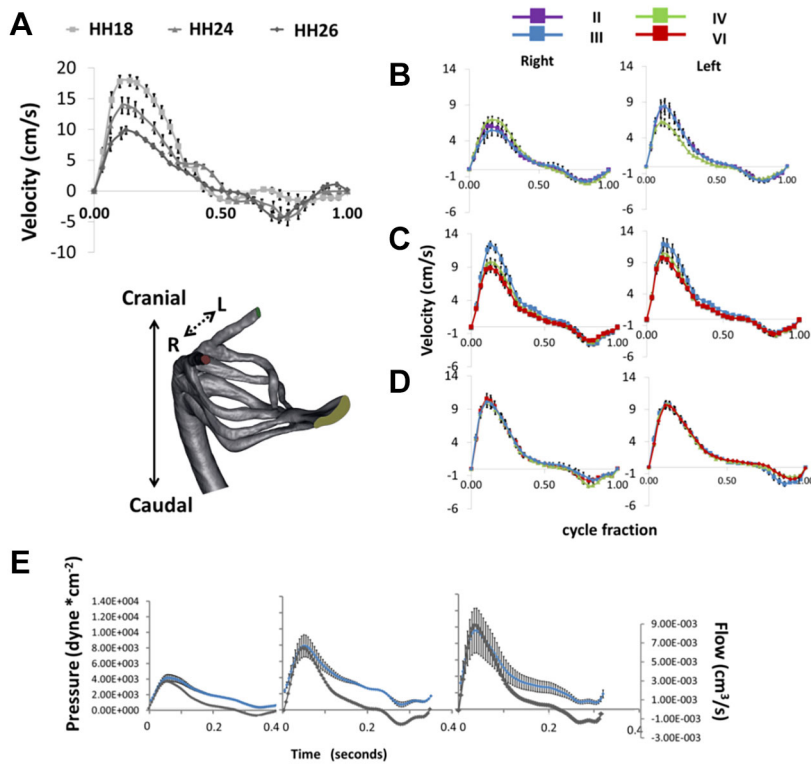
Fig. 10. Pulse wave Doppler velocity measurements of HH18, HH24 and HH26 embryos. Pulse wave measurements were obtained for OFTs, $n=8$ (HH18), $n=11$ (HH24) and $n=14$ (HH26) (A), and for PAAs at HH18 (B) HH24 (C) and HH26 (D). For HH18 summary curves, $n=12$ (PAA IVL), $n=13$ (PAA IIIL, IIR), $n=14$ (PAA IIL, IVR) and $n=15$ (PAA IIIR). For HH24 summary curves, $n=11$ for all PAAs. For HH26 summary curves, $n=13$ (PAA VIL, IVL, IIR) and $n=14$ (PAA IIIL, VIR, IVR). Of note are the side-specific, stage-specific similarities in both shape and velocity. (E) 3D-0D resulting inlet pressure (blue) and imposed inlet flow curves (black) for each of the stages. Standard error bars are shown in black for each curve. Because of the low velocity variation with each cohort, a single time-averaged curve was used for CFD inputs within a cohort.

a single value per arch, HH18 to HH26 WSS-surface area graphs follow a nonlinear function, monotonically increasing across stages (Fig. 9C). As hypothesized, a combination of pressure and WSS maps could account for many of the structural changes seen between stages over this critical window of development. Optimal WSS values may vary according to transmural pressure as determined by Pries et al. (1995). HH18 WSS zone of 80-160 dyne cm^{-2}, may therefore induce large area/diameter changes in HH18 embryos

(mean pressure per arch 3387 dyne cm^{-2}), but only slight deviations in HH24 embryos (mean pressure per arch 6964 dyne cm^{-2}). Pressure plays a key role in the cardiovascular system, as it must be large enough to push the necessary amount of blood through the arches and downstream vessels in order to meet the embryo's metabolic needs (Kowalski et al., 2012; Pries et al., 1998; Zamir, 1977). In addition to the embryo's metabolic need for function and growth, the transport system itself has a metabolic cost (wall tunica

Table 1. Least variability regions for combined hemodynamic area diameter changes along the arch arteries

	1	2	3	4	5	6	7	8	9	10
IIIR	P-D$_{min}$* P-Area* WSS-D$_{min}$* WSS-Area* WSS-D$_{max}$*							P-D$_{max}^{\ddagger}$ P-D$_{max}^{\S}$ WSS-D$_{max}^{\S}$		P-D$_{max}$*
IVR	WSS-D$_{max}^{\ddagger}$									
VIR	WSS-D$_{min}^{\S}$ WSS-Area§						P-D$_{min}^{\ddagger}$ WSS-D$_{min}^{\ddagger}$ WSS-Area‡	P-Area‡		P-D$_{min}^{\S}$ P-Area§
IIL		P-D$_{min}$*								
IIIL	WSS-D$_{min}$* WSS-Area* WSS-D$_{max}$*						WSS-D$_{max}^{\S}$	WSS-Area§	P-Area§	P-D$_{min}^{\ddagger}$ P-Area‡ WSS-D$_{min}^{\ddagger}$ WSS-Area‡ WSS-D$_{max}^{\ddagger}$
IVL		P-Area*				P-D$_{max}$*				P-D$_{max}^{\ddagger}$ P-D$_{min}^{\S}$ P-D$_{max}^{\S}$
VIL	WSS-D$_{min}^{\S}$									

Sections along the arches are numbered at the top. Least variable region per P-D$_{min}$, P-Area, P-D$_{max}$, WSS-D$_{min}$, WSS-Area, WSS-D$_{max}$ is calculated for each of the present stages.
*HH18, ‡HH24, §HH26 ($n=5$ embryos per stage).

media generation and blood volume maintenance) (Murray, 1926). PAA vessel morphology therefore results from an optimization process in which mechanical and metabolic stimuli trigger constant adaption (Kowalski et al., 2012; Murray, 1926; Pries et al., 1998; Taber, 1998).

To further characterize the effect/consequence of stage-specific variation in a 3D growth context, statistical shape modeling was used to transform the HH24 mean template into the HH26-slow and HH26-fast configurations. The overall displacement field magnitude remained the same for the HH24 to HH26-slow transformation at the level of the outflow tract (Fig. S6), which grew more in the vertical direction than the horizontal direction (unlike the longer more finessed HH26 and HH26-fast embryos). Although the HH26-slow outflow tract experiences the same magnitude of surface area displacement as the HH26 mean template embryo, the section of the arches most proximal to the heart experienced ~25% less surface area displacement. The mean displacement across the entire HH24 template to HH26-fast template displacement increased by ~21% (to 1.44). This increase was experienced more in the OFT than in the arches themselves. PAAs experienced a mean arch displacement of 0.73 (±0.16) cm between the large developmental transformation that is HH24 to HH26 growth. Their displacement maps support the theory of differential growth of the distal segments relative to the proximal.

A quantitative understanding of PAA growth and morphogenesis is necessary to uncover mechanisms of clinically significant outflow tract and great vessel malformations. These malformations involve substantial differential growth, rotations and motions of tissues formed from multiple cell lineages and in continuous engagement with complex hemodynamic environments. Purely genetic approaches lack the precision necessary, and even so quantitative tools for analyzing structure-function relationships across a population are sorely lacking. Here, we establish an integrated set of quantitative population-based morphological and hemodynamic analysis and simulation tools, and apply them to elucidate specimen-specific and group aggregate variations in flow, WSS and pressure. We quantified stage-specific vessel-specific functionality through resistance values. Results confirmed WSS as a major driver of PAA growth, and highlighted pressure as a secondary driver. Flow and pressure magnitudes increased dramatically across stages, while WSS magnitude was maintained. Side-specific flow dominance was not definite until HH26. Each stage was marked by a characteristic vessel shape that reflects the movement of the OFT and descending of the heart. By examining stage-specific characteristics as well as growth between stages from a number of perspectives, we define and quantify healthy PAA morphogenesis at this crucial stage of cardiac development. Ultimately, quantitatively interrogating variation in morphological outcomes is the best way to achieve new mechanistic insights into morphogenesis.

MATERIALS AND METHODS
Embryo culture and preparation
Fertile white Leghorn chicken eggs (Cornell Poultry Farm) were incubated blunt-side up for 3, 4 and 5 days in a continuous rocking incubator at 37.5°C. Embryos were randomly selected for each day endpoint for measurements and staging, geometric scanning, and modeling. This was intentional so as to study natural variation (that stems from genetic and epigenetic variability) within well-controlled conditions. In order to prepare embryos for geometric scanning, embryos were removed from the incubator at the appropriate stage and subsequently dissected away from their yolk sac. Injection micro-needles were fashioned from pulled capillary tubes (0.75 mm ID) cut to 20-35 μm inner diameter via a microforge (Glassworx). A micromanipulator

(model M3301L, World Precision Instruments) was used to position the needle into the apex of heart. The embryo's vascular system was flushed with phosphate-buffered solution followed by 4% paraformaldehyde to preserve inner vascular volumetric integrity. The embryos were then left in 4% paraformaldehyde for 24-48 h before being transferred to a 70% ethanol solution and stored (possibly for several weeks). Embryos were brought up to a 30% ethanol solution before being transferred to a diluted form of Lugol solution, aqueous potassium iodide and iodine (Sigma-Aldrich, L6146). The embryos were soaked in Lugol's and the solution was changed over several days until the embryos no longer took up any iodine. Embryos were then dehydrated down to 100% ethanol, placed in polymerase chain reaction tubes and sent to undergo 3-4 μm nano-computed tomography scans (nano-CT).

Ultrasound processing and generation of inlet flow curves
Outflow tract (OFT) velocity and that of the three paired pharyngeal arch arteries were measured using B-mode guided (Movie 1, Fig. 10) Doppler Ultrasound (Vevo770 and Vevo 2100, Visualsonics). Warm Earle's balanced salt solution was used as an aqueous conduit between the embryo and the ultrasound scanhead. Embryos were kept at 37.5°C during imaging by being placed in a heated water bath as previously noted (Yalcin et al., 2010). After imaging, the embryos were transferred back to the incubator and allowed to recover. For each analyzed stage, 11-15 Doppler recordings were averaged to obtain a summary velocity profile for each vessel of interest.

As Doppler ultrasound data only provide maximum velocity over time in a cross-section, additional information is needed to transform it into flow rate. More precisely, the velocity spatial profile is needed. In order to preserve arch velocity profiles, the maximum Doppler velocity measured at the distal region of the OFT could not be readily translated into inflow information. Instead, it was only used to obtain the velocity spatial profiles in the arches as follows. A Poiseuille inlet flow profile (Bharadwaj et al., 2012) was assumed for HH18 and HH24, respectively, while a plug inlet flow profile was assumed for HH26 (Bharadwaj et al., 2012) to first convert the OFT Doppler data into flow rate and apply this velocity information as an inlet boundary condition for an initial 3D CFD simulation, for which a ~90-10 flow split at the outlets was ensured. From there, the ratio between in silico flow and velocity calculated in each of the individual arches [$Q_{ref}/V_{max(ref)}$] was computed: this contains the velocity spatial profile information for each arch. A new Q_{inlet} was then calculated to be the sum of flow in each of the individual arches via the following equation:

$$Q_{inlet}(t) = \sum_{i=0}^{6} V_{imax}(t) \times \frac{Q_{i(ref)}}{V_{imax(ref)}}, \qquad (2)$$

where $V_{imax}(t)$ is the Doppler pulse wave velocity profile for that arch, ref refers to values measured in the initial simulation with Doppler imposed flow, and $Q_{i(ref)}/V_{imax(ref)}$ is an estimation of the profile contribution from each arch.

Zero-dimensional model
0D electric analog representations of the arch artery network were created for HH18, HH24 and HH26 geometries. Sundials initial value problem solver Implicit Differential-Algebraic solver, IDA (Lawerence Livermore National Laboratory, Livermore) was used to obtain solutions to the 0D circuit. The full 0D model consisted of the arch artery system, including the aortic sac inlet, three arch pairs, cranial and caudal sections of the DoA, and the distal components associated with these outlets, according to the geometry resulting from the 'In silico geometry preparation' section. The distal components (Fig. S4, dashed boxes), an RCR or Windkessel model, were adapted from Yoshigi et al.'s single compartment 0D model of HH18 and HH24 embryo circulation, as seen from the PAAs (Yoshigi et al., 2000). The values of the arch arteries and flow conduits that blood traveled through to reach the outlets were obtained from the 3D simulation. Iterations between the 0D and 3D-0D simulations were necessary to tune the 0D boundary conditions (detailed below in 'Multiscale 3D-0D simulations'), as shown by Pant et al. (2014). 0D representation of the HH18 and HH24 geometries are shown in Fig. S4. A separate 0D model exists for HH26 morphology where the onset of OFT septation requires that the aortic sac

resistance be divided into two. Resulting pressures after this division are labeled Ps1 and Ps2. 0D abstraction of the 3D domain is represented in black; the Windkessel boundary conditions are represented in red and outlined with dashed lines (Fig. 2, Fig. S4). Electric circuit models were updated after 3D simulations according to Ohms law.

In silico geometry preparation

Embryo-specific 3D geometries of the HH18 (day 3), HH24 (day 4) and HH26 (day 5) PAAs were generated by importing nano-CT images into MIMICS (Materialise) and 3MATICs (Materialise). PAA geometries extended from the distal outflow tract to the DoA and paired cranial aortae (Fig. 2). Geomagics Studio 10 (Geomagic) was also used for the preparation of 3D geometries for CFD. All embryos were scaled to account for the difference between dehydrated and native vessel size, as determined by a series of *in vivo* diameter verifications. India ink and Texas Red Dextran were used to obtain native vessel size across stages, results were compared with that of 3D reconstructions and a scaling factor was generated.

Multiscale 3D-0D simulations

Blood was treated as a Newtonian fluid with constant hemodynamic properties (ρ=1060 kg/m^3, μ=3.71×10^{-3} Pa.s) and rigid, impermeable vessel walls were assumed with no slip boundary conditions. Flow was simulated using the in-house code FELiScE (finite elements for life sciences and engineering; gforge.inria.fr/projects/felisce; Pant et al., 2014) on a high-resolution unstructured Cartesian grid with finite-element numerical treatment. For 3D mesh generation and adaptation, *feflo* and *ghs3d* (Loseille and Löhner, 2010) were used. Grid sensitivity analysis was conducted on a control PAA model for each stage in order to ensure consistency and reliability of the numerical solutions for all simulations presented in this study, beyond which resulting mass-flow redistributions were insensitive to further Cartesian grid refinements.

A natural flow profile was imposed at the inlet. To obtain this, an auxiliary steady Stokes equation, with natural boundary conditions at the outlets, is solved first (Pant et al., 2013). The resulting inlet velocity profile was subsequently scaled at each time-point to match the measured flow rate, in this case the flow resulting from Eqn 2. RCR Windkessel models are imposed at the outlets via explicit coupling, the differential equation for which is:

$$P + R_2 C \frac{dP}{dt} = (R_1 + R_2)Q + CR_1R_2 \frac{dQ}{dt}, \qquad (3)$$

where R_1 is the proximal resistance, R_2 is the distal resistance, C represents the capacitance, P is the pressure at the coupled interface and Q is the corresponding flow. Pressure values from the 0D model were used as initial estimates of the caudal and cranial pressures, allowing one cycle to sufficiently represent hemodynamic patterns at each stage. Parameters were tuned to ensure that the distribution of the total cardiac output to DoA and cranial vessels maintains a 90-10 flow-split over the course of one cycle (Hu and Clark, 1989; Wang et al., 2009) through a series of iterations, as mentioned above ('Zero-dimensional model' section). Briefly, initial RCR parameters were calculated directly from the Yoshigi model (Yoshigi et al., 2000), an initial 3D-0D simulation was run, flow splits were checked and the full 0D model parameters were updated with the results of the 3D simulation. The RCR parts of the 0D model were then tuned until a 90-10 split was obtained for the numerically calculated flow values and the 3D-0D model was then updated. This process was repeated until a 90-10 split was obtained for the 3D-0D simulation. Caudal bounds were fixed to maintain stage-specific DoA pressure values. All flows were laminar with Reynolds numbers less than 3 at the distal region of the OFT and Womerseley numbers less than 7. Womerseley numbers were less than 1 across all arch arteries.

Hemodynamic and morphological post-processing
Geometric measurements and flow visualization

The Vascular Modeling Toolkit (vmtk), supported by Orobix Srl, was used to obtain cross-sectional area and diameter measurements taken along the centerline of each geometry (Piccinelli et al., 2009). Once the centerline was obtained, normal and tangent functions were calculated for one in three points along the centreline, in order to obtain the equation of a plane normal to the centerline at each point. Each section was imported into Ensight and its orientation verified before calculations were performed. Ensight (Computational Engineering International), was used for all post-processing, visualization and measurement of flow properties.

Pulsatility was taken to be pressure at peak flow minus the pressure at the minimum flow ($P_{max}-P_{min}$). Pressure drop was taken to be average pressure in the most proximal end of a segment minus average pressure in the distal end of a segment. An equivalent resistance value (R_{eq}) was calculated across stages according to Eqn 1. P_{in} was taken to be pressure at the OFT. P_{out} was taken as a combination of the three outlet pressures (left cranial, right cranial and caudal dorsa aorta outlets) multiplied by their respective flow distribution.

Statistical shape modeling

Deformetrica (Durrleman et al., 2014) statistical shape modeling software was used to create stage-specific average PAA surfaces and to grow one stage-specific cohort to the next. The averaged geometrical surface served as a template for mapping morphological characteristics to the surface for each of the HH18, HH24 and HH26 geometries. Registration was also performed between the HH18 and HH24 templates, as well as between the HH24 and HH26 templates. The HH18 template was then deformed towards the HH24 template geometry and the HH24 template deformed towards the HH26 template through a combination of distance minimization and transformation algorithms driven by moment vectors over the ambient space. Through the statistical shape modeling software, geometrical surfaces do not need point-by-point mesh correspondence, and their dissimilarity is evaluated by a metric on a mathematical current (flux of a vector field) framework that deforms the underlying 3D space, rather than on anatomical landmarks themselves. This non-parametric technique allows for the handling of complex amorphous structures, and is particularly well suited for congenital heart defect models (Guibert et al., 2014). At the basis of this non-parametric comparison are currents. Currents characterize a shape as a distribution of shape features. Surfaces are embedded in 3D space and shape variations are measured based on deformations of the underlying 3D space. Shapes are compared by computing how distributions of features differ. In the 'forward approach', which is applied by this model, each subject is a deformation of the anatomical mean shape (the template) plus a residual (shape features not represented by the template). The deformations are described by diffeomorphisms or functions that preserve the topology of an object, mapping one manifold (the template) to another in a continuous fashion. Computational surface meshes serve as inputs into the model. A mean template is iteratively computed as an average of all currents. At each iteration, the present template is registered to each of the study's subjects, computing the individual deformation. A new template is computed through a deformation in order to minimize the distance between the (newly) deformed template and target shape object (individual subject). A transformation function maps the template towards each individual subject shape, allowing each individual subject to be characterized by a multitude of deformation vectors rather than its actual 3D surface. This technique is called large deformation diffeomorphic metric mapping.

Statistical analysis

Morphological and hemodynamic changes were compared qualitatively and quantified when possible. Results were summarized in the form of mean and s.d. values over the course of one cardiac cycle. Paired *t*-tests were used where appropriate with $P<0.05$ denoting significance. Linear regressions and exponential decays were performed.

Statistical comparisons were made using GraphPad Prism. Linear regressions were plotted on hemodynamic versus geometrical parameter graphs for each of the HH18, HH24 and HH26 stages. The Friedman test was used to test for significant differences between HH26 arch subgroups. The Mann–Whitney *U*-test was used for flow split validation. Friedman's test is a nonparametric test used to compare three or more paired groups and by ranking the values within groups and then providing a one-way analysis of variance.

In order to summarize local stage-specific features, local RSD and deviation from mean values were calculated based on a point-by-point

comparison throughout the arches. RSD was taken to the specific value divided by the average value across embryos (specific value/mean value). Deviation from the mean was taken to be the specific value minus the mean normalized to the mean (specific value−mean value)/mean value. Values for each arch were taken at ten locations along the arch, from beginning to end. In this way, values were compared at relative position, rather than at a precise distance for both morphological and hemodynamic parameters.

References
Abu-issa, R., Smyth, G., Smoak, I., Yamamura, K. and Meyers, E. N. (2002). Fgf8 is required for pharyngeal arch and cardiovascular development in the mouse. *Development* **4625**, 4613-4625.

Banerjee, I., Carrion, K., Serrano, R., Dyo, J., Sasik, R., Lund, S., Willems, E., Aceves, S., Meili, R., Mercola, M. et al. (2015). Cyclic stretch of embryonic cardiomyocytes increases proliferation, growth, and expression while repressing Tgf-β signaling. *J. Mol. Cell. Cardiol.* **79**, 133-144.

Beloussov, L. V. (2008). Mechanically based generative laws of morphogenesis. *Phys. Biol.* **5**, 015009.

Bharadwaj, K. N., Spitz, C., Shekhar, A., Yalcin, H. C. and Butcher, J. T. (2012). Computational fluid dynamics of developing avian outflow tract heart valves. *Ann. Biomed. Eng.* **40**, 2212-2227.

Brownlee, R. D. and Langille, B. L. (1991). Arterial adaptations to altered blood flow. *Can. J. Physiol. Pharmacol.* **69**, 978-983.

de Bakker, B. S., de Jong, K. H., Hagoort, J., de Bree, K., Besselink, C. T., de Kanter, F. E., Veldhuis, T., Bais, B., Schildmeijer, R., Ruijter, J. M. et al. (2016). An interactive three-dimensional digital atlas and quantitative database of human development. *Science* **354**, aag0053.

Durrleman, S., Prastawa, M., Charon, N., Korenberg, J. R., Joshi, S., Gerig, G. and Trouvé, A. (2014). Morphometry of anatomical shape complexes with dense deformations and sparse parameters. *Neuroimage* **101**, 35-49.

Fung, Y. (1997). *Biomechanics Circulation*. 2nd edn. Heidelberg, Germany: Springer.

Go, A. S., Mozaffarian, D., Roger, V. L., Benjamin, E. J., Berry, J. D., Borden, W. B., Bravata, D. M., Dai, S., Ford, E. S., Fox, C. S. et al. (2013). Executive summary: heart disease and stroke statistics–2013 update: a report from the American Heart Association. *Circulation* **127**, 143-152.

Guibert, R., McLeod, K., Caiazzo, A., Mansi, T., Fernández, M. A., Sermesant, M., Pennec, X., Vignon-Clementel, I. E., Boudjemline, Y. and Gerbeau, J.-F. (2014). Group-wise construction of reduced models for understanding and characterization of pulmonary blood flows from medical images. *Med. Image Anal.* **18**, 63-82.

Hiruma, T. and Hirakow, R. (1995). Formation of the pharyngeal arch arteries in the chick embryo. Observations of corrosion casts by scanning electron microscopy. *Anat. Embryol.* **191**, 415-423.

Hiruma, T., Nakajima, Y. and Nakamura, H. (2002). Development of pharyngeal arch arteries in early mouse embryo. *J. Anat.* **201**, 15-29.

Hogers, B., DeRuiter, M. C., Gittenberger-de Groot, A. C. and Poelmann, R. E. (1997). Unilateral vitelline vein ligation alters intracardiac blood flow patterns and morphogenesis in the chick embryo. *Circ. Res.* **80**, 473-481.

Hogers, B., DeRuiter, M. C., Gittenberger-de Groot, A. C. and Poelmann, R. E. (1999). Extraembryonic venous obstructions lead to cardiovascular malformations and can be embryolethal. *Cardiovasc. Res.* **41**, 87-99.

Hu, N. and Clark, E. B. (1989). Hemodynamics of the stage 12 to stage 29 chick embryo. *Circ. Res.* **65**, 1665-1670.

Hu, N., Christensen, D. A., Agrawal, A. K., Beaumont, C., Clark, E. B. and Hawkins, J. A. (2009). Dependence of aortic arch morphogenesis on intracardiac blood flow in the left atrial ligated chick embryo. *Anat. Rec.* **292**, 652-660.

Jaffee, O. C. (1965). Hemodynamic factors in the development of the chick embryo heart. *Anat. Rec.* **151**, 69-75.

Kamiya, A. and Togawa, T. (1980). Adaptive regulation of wall shear stress to flow change in the canine carotid artery. *Am. Physiol. Soc.* **239**, H14-H21.

Kowalski, W. J., Teslovich, N. C., Dur, O., Keller, B. B. and Pekkan, K. (2012). Computational hemodynamic optimization predicts dominant aortic arch selection is driven by embryonic outflow tract orientation in the chick embryo. *Biomech. Model. Mechanobiol.* **11**, 1057-1073.

Kowalski, W. J., Dur, O., Wang, Y., Patrick, M. J., Tinney, J. P., Keller, B. B. and Pekkan, K. (2013). Critical transitions in early embryonic aortic arch patterning and hemodynamics. *PLoS ONE* **8**, e60271.

Kowalski, W. J., Pekkan, K., Tinney, J. P. and Keller, B. B. (2014). Investigating developmental cardiovascular biomechanics and the origins of congenital heart defects. *Front. Physiol.* **5**, 408.

Langille, B. and O'Donnell, F. (1986). Reductions in arterial diameter produced by chronic decreases in blood flow are endothelium-dependent. *Science* **231**, 405-407.

Leatherbury, L., Braden, D. S., Tomita, H., Gauldin, H. E. and Jackson, W. F. (1990a). Hemodynamic changes. Wall stresses and pressure gradients in neural crest-ablated chick embryos. *Ann. N. Y. Acad. Sci.* **588**, 305-313.

Leatherbury, L., Gauldin, H. E., Waldo, K. and Kirby, M. L. (1990b). Microcinephotography of the developing heart in neural crest-ablated chick embryos. *Circulation* **81**, 1047-1057.

Li, Z., Huang, W., Jiang, Z. L., Gregersen, H. and Fung, Y.-C. (2004). Tissue remodeling of rat pulmonary arteries in recovery from hypoxic hypertension. *Proc. Natl. Acad. Sci. USA* **101**, 11488-11493.

Lin, I.-E. and Taber, L. A. (1995). A model for stress-induced growth in the developing heart. *J. Biomech. Eng.* **117**, 343-349.

Lindsey, S. E., Menon, P. G., Kowalski, W. J., Shekhar, A., Yalcin, H. C., Nishimura, N., Schaffer, C. B., Butcher, J. T. and Pekkan, K. (2015). Growth and hemodynamics after early embryonic aortic arch occlusion. *Biomech. Model. Mechanobiol.* **14**, 735-751.

Loseille, A. and Löhner, R. (2010). Anisotropic adaptive simulations in aerodynamics. In *48th AIAA Aerospace Sciences Meeting Including the New Horizons Forum and Aerospace Exposition.* American Institute of Aeronautics and Astronautics.

Manner, J. (2000). Cardiac looping in the chick embryo: a morphological review with special reference to terminological and biomechanical aspects of the looping process. *Anat. Rec.* **259**, 248-262.

Molin, D. G. M., DeRuiter, M. C., Wisse, L. J., Azhar, M., Doetschman, T., Poelmann, R. E. and Gittenberger-de Groot, A. C. (2002). Altered apoptosis pattern during pharyngeal arch artery remodelling is associated with aortic arch malformations in Tgfbeta2 knock-out mice. *Cardiovasc. Res.* **56**, 312-322.

Mozaffarian, D., Benjamin, E. J., Go, A. S., Arnett, D. K., Blaha, M. J., Cushman, M., Das, S. R., Ferranti, S., De Després, J. et al. (2016). AHA statistical update heart disease and stroke statistics — 2016 update a report from the American Heart Association. *Circulation* **133**, e38-360.

Murray, C. D. (1926). The physiological principle of minimum work. I. The vascular system and the cost of blood volume. *Physiology* **12**, 207-214.

Pant, S., Fabrèges, B., Gerbeau, J.-F. and Vignon-Clementel, I. E. (2013). A multiscale filtering-based parameter estimation method for patient-specific coarctation simulations in rest and exercise. In *Statistical Atlases and Computational Models of the Heart. Imaging and Modelling Challenges: 4th International Workshop, STACOM 2013, Held in Conjunction with MICCAI 2013, Nagoya, Japan, September 26, 2013*. pp. 102-109. Heidelberg, Germany: Springer.

Pant, S., Fabrèges, B., Gerbeau, J. and Vignon-Clementel, I. E. (2014). A methodological paradigm for patient-specific multi-scale CFD simulations: from clinical measurements to parameter estimates for individual analysis. *Int. J. Numer. Methods Biomed. Eng.* **30**, 1614-1648.

Piccinelli, M., Veneziani, A., Steinman, D. A., Remuzzi, A. and Antiga, L. (2009). A framework for geometric analysis of vascular structures: application to cerebral aneurysms. *IEEE Trans. Med. Imaging* **28**, 1141-1155.

Pries, A. R., Secomb, T. W. and Gaehtgens, P. (1995). Design of vascular beds. *Circ. Res.* **77**, 1017-1023.

Pries, A. R., Secomb, T. W. and Gaehtgens, P. (1998). Structural adaptation and stability of microvascular networks: theory and simulations. *Am. J. Physiol.* **275**, H349-H360.

Rana, M. S., Sizarov, A., Christoffels, V. M., Moorman, A. F. M. and Al, R. E. T. (2014). Development of the human aortic arch system captured in an interactive three-dimensional reference model. *Am. J. Med. Genet.* **164A**, 1372-1383.

Rychter, Z. (1962). Experimental morphology of the aortic arches and the heart loop in chick embryos. *Adv. Morphog.* **2**, 333-371.

Rychter, Z., Kopecky, M. and Lemez, L. (1955). A micromethod for determination of the circulating blood volume in chick embryos. *Nature* **175**, 1126-1127.

Sedmera, D., Pexieder, T., Rychterova, V., Hu, N. and Clark, E. B. (1999). Remodeling of chick embryonic ventricular myoarchitecture under experimentally changed loading conditions. *Anat. Rec.* **254**, 238-252.

Sinibaldi, G. and Romano, G. P. (2017). Flow configurations in a Y splitting-junction microchannel. *Fluids* **2**, 18.

Taber, L. A. (1995). Biomechanics of growth, remodeling, and morphogenesis. *Appl. Mech. Rev.* **48**, 487.

Taber, L. A. (1998). An optimization principle for vascular radius including the effects of smooth muscle tone. *Biophys. J.* **74**, 109-114.

Taber, L. A. (2009). Towards a unified theory for morphomechanics. *Philos. Trans. R. Soc. A* **367**, 3555-3583.

Taber, L. A. and Eggers, D. W. (1996). Theoretical study of stress-modulated growth in the aorta. *J. Theor. Biol.* **180**, 343-357.

Waldo, K., Miyagawa-Tomita, S., Kumiski, D. and Kirby, M. L. (1998). Cardiac neural crest cells provide new insight into septation of the cardiac outflow tract: aortic sac to ventricular septal closure. *Dev. Biol.* **196**, 129-144.

Wang, Y., Dur, O., Patrick, M. J., Tinney, J. P., Tobita, K., Keller, B. B. and Pekkan, K. (2009). Aortic arch morphogenesis and flow modeling in the chick embryo. *Ann. Biomed. Eng.* **37**, 1069-1081.

Wendling, O., Dennefeld, C., Chambon, P. and Mark, M. (2000). Retinoid signaling is essential for patterning the endoderm of the third and fourth pharyngeal arches. *Development* **1562**, 1553-1562.

Yalcin, H. C., Shekhar, A., Nishimura, N., Rane, A. A., Schaffer, C. B. and Butcher, J. T. (2010). Two-photon microscopy-guided femtosecond-laser photoablation of avian cardiogenesis: noninvasive creation of localized heart defects. *Am. J. Physiol. Heart Circ. Physiol.* **299**, H1728-H1735.

Yashiro, K., Shiratori, H. and Hamada, H. (2007). Haemodynamics determined by a genetic programme govern asymmetric development of the aortic arch. *Nature* **450**, 285-288.

Yoshigi, M., Knott, G. D. and Keller, B. B. (2000). Lumped parameter estimation for the embryonic chick vascular system: a time-domain approach using MLAB. *Comput. Methods Programs Biomed.* **63**, 29-41.

Zahka, K. G., Hu, N., Brin, K. P., Yin, F. C. P. and Clark, E. B. (1989). Aortic impedance and hydraulic power in the chick embryo from stages 18 to 29. *Circ. Res.* **64**, 1091-1095.

Zamir, M. (1977). Shear Forces and Blood Vessel Radii in the Cardiovascular System. *J. Gen. Physiol.* **69**, 449-461.

DEVELOPMENT